1 **The influence of sea- and land-breeze circulations on the diurnal variability of precipitation**

2 **over a tropical island**

4 Lei Zhu[1,2,3], Zhiyong Meng[1]*, Fuqing Zhang[2,3], Paul M. Markowski[2]

6 *[1]Laboratory for Climate and Ocean-Atmosphere Studies, Department of Atmospheric and*

7 *Oceanic Sciences, School of Physics, Peking University, Beijing, China*

8 *[2]Department of Meteorology and Atmospheric Science, The Pennsylvania State University,*

9 *University Park, Pennsylvania*

10 *[3] Center for Advanced Data Assimilation and Predictability Techniques, The Pennsylvania State*

11 *University, University Park, Pennsylvania*

Corresponding author address: Dr. Zhiyong Meng, Laboratory for Climate and Ocean–Atmosphere Studies, Department of Atmospheric and Oceanic Sciences, School of Physics, Peking University, Beijing, China.

E-mail: zymeng@pku.edu.cn

Abstract

15   This study examines the diurnal variation of precipitation over Hainan island in the South

16   China Sea using gauge observations from 1950 to 2010 and CMORPH satellite estimates from

17   2006 to 2015, as well as numerical simulations which is the first time to use climatological mean

18   initial conditions and diurnally averaged periodic lateral boundary conditions to study the dynamic

19   and thermodynamic processes (and the impacts of land-sea breeze circulations) that control the

20   rainfall distribution and climatology. Precipitation is most significant from April to October, and

21   exhibits a strong diurnal cycle resulting from land/sea breeze circulations. More than 60% of the

22   total annual precipitation over the island is attributable to the diurnal cycle with a significant

23   monthly variability as well. The CMORPH and gauge datasets agree well, except that the

24   CMORPH data underestimates precipitation and has a 1-h delay of peaks. The diurnal cycle of the

25   rainfall and the related land/sea breeze circulations during May and June were well captured by

26   convection-permitting numerical simulations with WRF, which were initiated from 10-year

27   average ERA-interim reanalysis. The simulations have a slightly overestimation of rainfall

28   amounts and a 1-h delay in peak rainfall time. The diurnal cycle of precipitation is driven by the

29   occurrence of moist convection around noontime owing to low-level convergence associated with

30   the sea breeze circulations. The precipitation intensifies rapidly thereafter and peaks in the

31   afternoon with the collisions of sea breeze fronts from different sides of the island. Cold pools of

32   the convective storms contribute to the inland propagation of the sea breeze. Generally,

33   precipitation dissipates quickly in the evening due to the cooling and stabilization of the lower

34   troposphere and decrease of boundary-layer moisture. Interestingly, the rather high island

35   orography is not a dominant factor in the diurnal variation of the precipitation over the island.

1. Introduction

On tropical islands, the diurnal precipitation cycle tends to be driven by the land-sea breeze (LSB), as well as mountain-valley wind systems (Mapes et al. 2003; Qian 2008; Crosman and Horel 2010). Both rain gauge and satellite observations indicate that rainfall peaks in the late afternoon over inland regions, and in the early morning or evening offshore (Yang and Slingo 2001).

The emergence of high temporal and spatial resolution satellite-estimated precipitation observations, such as those provided by Tropical Rainfall Measuring Mission (TRMM, Huffman et al. 2007) and Climate Prediction Center Morphing Technique (CMORPH, Joyce et al. 2004), has greatly improved our understanding of tropical precipitation. Precipitation amounts are much higher over tropical islands than their surrounding oceans (Qian 2008). More than 34% of the total precipitation in the tropics is attributable to precipitation over land (Ogrino et al. 2016). Moreover, the tropical precipitation is usually due to convection (Dai 2001), and tropical convection is well known to have an important influence on the large-scale atmospheric circulation (Neale and Slingo 2003; Sobel et al. 2011).

Many efforts have been made to understand the mechanisms behind the diurnal precipitation cycle over tropical islands. With CMORPH data and regional climate model simulation, Qian (2008) found that sea-breeze convergence, mountain-valley winds and cumulus merger process are the predominant reasons for the diurnal precipitation cycles while the underrepresentation of islands and terrain results in the precipitation underestimate. Hassim et al. (2016) examined the diurnal cycle of rainfall over New Guinea with a 4-km convection-permitting WRF model. They found the importance of the sea breeze in the initiation of rainfall but focused on large-scale atmospheric properties preferential to the propagation of systems offshore at night. They also

60 found that orography and the coastline along with gravity waves were beneficial for the longevity

61 and maintenance of the convection systems though they are not the fundamental reasons for the

62 convection initiation.

63 The diurnal cycle of tropical rainfall is usually poorly captured by most global climate

64 models (GCMs) and even cloud-resolving models (CRMs), owing to model uncertainties in

65 depicting the physical mechanisms that underlie the diurnal precipitation cycle (Yang and Slingo

66 2001; Qian 2008; Nguyen et al. 2015). Yang and Slingo (2001) found that the deficiency of model's

67 physical parameterizations may be the main reason for the difficulty in capturing the observed

68 phase of diurnal cycle in convection. Diurnal variability is only captured in some places or months

69 where the signals are strong, while at other times, the diurnal signals are captured, but with a large

70 timing error of the maxima and minima. Studies show that the LSB may have different

71 contributions to the diurnal variabilities of precipitation at different places (Keenan et al. 1988;

72 Qian 2008; Wapler and Lane 2012; Chen et al. 2017). Precipitation tends to be initiated by the

73 convergence of land breezes (Wapler and Lane 2012) and sea breezes (Qian 2008) over gulf area

74 and islands area, respectively. Interactions between land breeze and prevailing wind are likely to

75 produce precipitation over the coast area or tropical islands (Keenan et al. 1988; Chen et al. 2017).

76 Recent studies (Bao et al. 2013; Chen et al. 2016, 2017) also have found that convectively driven

77 cold pools and latent cooling, as well as environmental wind and moisture, may play important

78 roles in the propagation and maintenance of diurnal rainfall in coastal regions. How cold pools and

79 latent cooling affect the diurnal cycle of rainfall and related LSB over a tropical island has not

80 been studied extensively.

81 This current work is aimed at examining the diurnal cycle of precipitation and the related

82 LSB over Hainan Island in the South China Sea. Hainan Island is a tropical island located off the

83   southern coast of China (Fig.1). It is one of the rainiest areas in China, and is influenced by a

84   variety of synoptic-scale and mesoscale weather systems, such as monsoon, tropical cyclones, LSB,

85   and mountain-plain solenoids. The island's topography features mountains in the southwest, with

86   peak altitude of approximately 1000 meter above the sea level (shaded in Fig. 1), and plains in the

87   northeast.

88   The characteristics of precipitation and LSB over Hainan Island have been examined via

89   statistical methods based on either surface observation or modeling simulations (Tu et al. 1993;

90   Zhai et al. 1998; Zhang et al. 2014; Liang and Wang 2016). Based on nine station-based wind

91   observations, Zhang et al. (2014) found that LSB occurs more frequently in summer and autumn,

92   though their findings are limited in using observations in only one month of one season. Most

93   recently, Liang and Wang (2016) examined the relationship between the sea breeze and

94   precipitation of Hainan Island using surface wind and precipitation observations along with the

95   global reanalysis over several years. They hypothesized that the seasonal precipitation is due to

96   the initiation of convection by the LSB, but they did not provide thorough investigation on how

97   the LSB circulations trigger and enhance the precipitation over Hainan Island.

98   The objective of this study is to investigate the diurnal precipitation variation over Hainan

99   Island and the detailed physical mechanisms related to LSB forcing and variability. This is the first

100   time using semi-idealized convection-permitting simulations with climatological mean initial

101   conditions and diurnally averaged periodic lateral boundary conditions to study the dynamic and

102   thermodynamic processes (and the impacts of land-sea breeze circulations) that control the rainfall

103   distribution and climatology over a tropical island. We would also highlight the removal of terrain

104   effect, along with a further simplification using a perfect oval shaped island. The study relies on

105   rain gauge observations and satellite-derived precipitation estimates, as well as convection-

106   permitting numerical simulations. Section 2 describes the dataset and the methodology. Section 3

107   documents the diurnal precipitation variation in each month, as well as the percentage of the total

108   precipitation that can be attributed to the diurnal cycle. The relationship between the precipitation

109   and surface winds during the first rainy season [May and June, which is defined relative to the

110   second rainy season (July through September) of southern China when precipitation is mainly

111   caused by typhoons] are also analyzed. The model configuration and results of the simulations are

112   presented in Section 4. Conclusions are presented in Section 5.

113

114   **2. Observation dataset and methodology**

115   Rainfall was analyzed using 19 rain gauges on Hainan Island (Fig. 1). The gauges are

116   relatively evenly distributed across the island. The sampling frequency is one hour, which is dense

117   enough to represent the diurnal precipitation variation over the island. The dataset spans 60 years

118   (1951–2010), though full records exist for only a subset of this period at some of the stations,

119   owing to the fact that the stations were built at different times (the detailed dataset periods for each

120   station are shown in Table 1). Surface temperature and wind observations obtained at the same

121   locations over a four-year period (2007–2010) were used to investigate the land and sea breezes.

122   The surface precipitation observations are augmented by National Oceanic and Atmospheric

123   Administration (NOAA) and Climate Prediction Center Morphing Technique (CMORPH) data

124   derived from low-Earth orbiting and geostationary satellites (Joyce et al. 2004). The CMORPH

125   grid with a temporal resolution of 30 minutes is 0.7277 degree by 0.7277 degree (approximately 8

126   km by 8 km). Ten years of CMORPH data (2006–2015) were used.

127   A series of convection-permitting numerical simulations were performed with the Advanced

128   Research Weather Research and Forecasting (ARW, Skamarock et al. 2008) model version 3.7.1

129   to investigate dynamical features of the diurnal cycle of precipitation and its physical mechanisms

130   in particular with regards to LSB forcing. Initial and lateral boundary conditions were provided by

131   the European Center for Medium-Range Weather forecast Interim (ERA-interim) reanalysis data

132   (Dee et al. 2011) of 0.75° × 0.75° grid spacing. Only one domain was used with 225 × 205 grid

133   points and a horizontal grid spacing of 2 km. A total of 50 vertical levels were used with the model

134   top at 50 hPa. The Yonsei University (YSU) boundary scheme (Hong et al. 2006), Dudhia

135   shortwave radiation (Dudhia 1989), the Rapid Radiative Transfer Model longwave radiation

136   scheme (Iacono et al. 2008), the single-moment 5-class microphysics (Hong et al. 2004), five-layer

137   thermal diffusion land surface and Revised MM5 surface layer schemes were used, while no

138   cumulus parameterization was used in this study.

139   The initial conditions of all simulations were the average of ERA-interim reanalysis data at

140   0000 UTC in May and June of 2006–2015. The lateral boundary conditions were obtained in the

141   same way as the initial conditions, cycled from 0000 to 0600, 1200, 1800 and 0000 UTC.

142   Experiment REAL was initiated with the unmodified initial and lateral boundary conditions to

143   simulate the diurnal characteristics. Experiment NoTER is the same as REAL except that the

144   orography over Hainan Island is removed in the initial conditions in order to isolate the influence

145   of the island's terrain. Simplifying the influences of land category and coastline, experiment

146   IDEAL was constructed with an idealized elliptical island to replace the real Hainan Island in the

147   initial condition. The idealized island has a similar size and orientation, and is located at the same

148   place as Hainan Island (Fig. 1), covered with uniform grassland (LU_INDEX=7 in WRF model)

149   while other areas of the model domain are set as ocean. In order to examine the impact of latent

150   heating/cooling on the LSB and related rainfall, sensitivity experiment FakeDry was performed

151   similar to the IDEAL experiment, except for turning off latent heating and cooling in the model

152   (no_mp_heating=1 in WRF model). Another sensitivity experiment NOVAP was performed

153   similar to IDEAL experiment except for turning off the evaporation of liquid water, which prevents

154   the cold pool generation from moisture convection process. A similar methodology has been used

155   to study diurnal cycle of precipitation in many different regions (Trier et al. 2010; Sun and Zhang

156   2012; Bao and Zhang 2013; Chen et al. 2016, 2017). The biggest advantage of this method is that

157   it is able to capture the general characteristics of the diurnal cycle of precipitation and the related

158   dynamical processes instead of just focusing on a single case. All simulations were integrated for

159   one month. The mean over the last 26 days was used for the analyses in order to alleviate the spin-

160   up issue and day-to-day variability.

161

162   **3. Observation analysis**

163   **3.1. Diurnal variation of precipitation and its seasonal-dependent features**

164   Diurnal variations of precipitation were examined at each single station in each month based

165   on the hourly gauge precipitation observation averaged over the period from 1951 to 2010. The

166   hourly precipitation evolution shows a significant seasonal cycle over the island. Most of the

167   precipitation falls from April to October, which is the monsoon season, and exhibits a distinct

168   diurnal cycle during that period, whereas less precipitation and lack of a strong diurnal cycle

169   characterize the other months (Fig. 2). The seasonal variability is related to the annual cycle of the

170   East Asian Monsoon. April and September are the two transitional periods of the low-level

171   prevailing wind; the prevailing wind strongly influences the transport of water vapor and

172   precipitation.

173   The diurnal precipitation cycle has the maximum precipitation at 1500 local standard time

174   (LST, LST=UTC+8) in most months during the warm season, except at 1600 LST in April and

175   July. No second precipitation peak is observed, which is different from studies of other tropical

176   islands in which a second peak between midnight and early morning has been noted (Kishtawal

177   and Krishnamurti 2001; Wapler and Lane 2012). The second nocturnal peak was found to be

178   closely related to convection caused by mountain-plains solenoid that propagates offshore and

179   coincides with the land breeze during the night or early morning.

180   The diurnal precipitation cycle shows location-dependent features (Fig. 2). We grouped the

181   stations with different colors based on their similarity in diurnal variations which to a large extent

182   are correlated with their geographical locations. No heavy rainfall or distinct variability is observed

183   at stations along the southern coastline (blue dots on Fig. 1 and blue lines on Fig. 2). All the rest

184   of the island stations share similar diurnal peak precipitation times with the red-dot stations (in red

185   lines) having the highest peak values from April to July while in August and September both the

186   red-dot and black-dot stations (mostly inland) share strongest peaks.

187   Even though the distribution of gauge-based precipitation station is relatively even across the

188   island, the observations are still too sparse to analyze the detailed rainfall pattern over the island.

189   For this reason, satellite-derived precipitation CMORPH data were also used to examine the

190   diurnal rainfall variation for each of the 19 gauge stations. The hourly diurnal precipitation

191   variation derived from the CMORPH data agrees well with the rain gauge observations in each

192   month (Fig. 3), though the CMORPH amounts are slightly smaller. The time of peak precipitation

193   in the warm season (from May to August) is delayed by one hour in most months in the CMORPH

194   data (maximum at 1600 LST) relative to the peak in the gauge-based observations. These results

195   indicate good agreement between the CMORPH data and gauges, in particular for the warm-season

196   months that are the focus of this study.

197   The percentage of the diurnal precipitation in the total precipitation over the island in each

198   month was examined with the CMORPH data (Fig. 4). Similar to He and Zhang (2010) and Bao

199   et al. (2011), the diurnal precipitation percentage was defined as the mean rainfall rate at each 1-

200   hour interval by diurnal precipitation percentage $=\frac{\sum_{t=0}^{23}|(r_t-\bar{r})|}{r_d}$, in which, r_t is the mean hourly

201   precipitation at each hour t (0–23), $\bar{r}$ is the mean hourly precipitation at all hours, and the r_d is the

202   daily mean precipitation. The diurnal precipitation percentage represents a large percentage of the

203   total precipitation over the island in most months (Fig. 4). In particular, the total precipitation in

204   May is almost entirely attributable to the diurnal cycle (Fig. 4e). The diurnal contribution of the

205   total precipitation exceeds 60% averaged for the whole year and over the whole island, although

206   the magnitude is smaller in September and October. The diurnal precipitation percentage value

207   exceeds 20% in August and September (Figs. 4h and i). Moreover, the area exhibiting a large

208   magnitude of diurnal precipitation roughly coincides with the region also having the most

209   accumulated precipitation. However, the diurnal precipitation percentage is not quite related to the

210   precipitation intensity. The precipitation is extremely light in March and somewhat heavy in

211   September. However, the diurnal precipitation percentages are reversed (smaller percentages in

212   September, greater percentages in March), which is likely related to different physical processes

213   of the precipitation in those months. The detailed physical processes that lead to the steady

214   decrease of diurnal precipitation percentage from May to October before increasing again are

215   beyond the scope of the current study. The possible reasons could be attributed to the synoptic

216   scale storms, typhoons, prevailing winds, the land sea temperature contrast and atmospheric

217   moisture content, which will be explored in our future study.

218

219   **3.2. The diurnal cycle of precipitation, land breezes, and sea breezes in May and June**

220 A more detailed analysis of the diurnal rainfall variation in May and June was carried out

221 because of the intense hourly mean rainfall and high diurnal precipitation percentage. In May, the

222 prevailing warm and wet southwest monsoon airflow transports abundant moisture from the ocean

223 to Hainan Island. A distinct diurnal cycle of precipitation, with a single peak between 1200 and

224 2000 LST, is evident in both the gauge-based and CMORPH data (Fig. 5). The datasets agree well

225 with each other at each surface station, except that CMORPH data exhibit larger peak values at the

226 red and green stations. Four gauge-based stations in blue have a much weaker daytime peak. These

227 stations, however, have an apparent nocturnal peak, whereas other stations do not exhibit a

228 nocturnal peak. The nocturnal precipitation is possibly attributable to the convergence between the

229 low-level prevailing wind and downhill jet circulations, which are to be examined with the

230 numerical simulations in section 4. The average over all stations (thick black line in Fig. 5) also

231 exhibits an obvious diurnal cycle.

232 The horizontal distribution of precipitation was analyzed using the CMORPH data (every 3 h

233 except for using 1700 LST as it is the strongest rainfall time in CMORPH data in Fig. 6) along

234 with the perturbation surface wind at gauge stations, which was obtained by subtracting the daily

235 mean from the total wind to highlight the diurnal cycle. The precipitation averaged over all times

236 shows that the precipitation mainly appears in the northeast in the lee-side of mountainous area

237 (Fig. 6a). The gauge-based stations with significant diurnal cycle (in red dots) are located over the

238 heaviest rainfall region while the gauge-based stations with non-distinctive diurnal feature (in blue

239 dots) are located in the weakest precipitation area. Hourly variation of precipitation shows that

240 there is little precipitation over the island in the early to mid-morning (0000 to 0900 LST), which

241 is on average less than that over the surrounding ocean. At 0600 LST, the perturbation surface

242 wind at gauge stations has an offshore direction in coastal area, a signature of nighttime land breeze

243 (Fig. 6b). Three hours later at 0900 LST, the perturbation wind strengthens and turns to the right

244 of its previous direction, particularly along the coast (Fig. 6c). At 1200 LST, the wind has changed

245 to onshore direction representing the beginning of sea breeze, along with the start of weak inland

246 precipitation where the sea breeze converges (Fig. 6d). In the next several hours (Figs. 6e–f), the

247 rainfall intensifies rapidly, reaching to the peak at around 1700 LST. The heaviest precipitation

248 concentrates in the northeast island corresponding to strong convergence of sea breeze (Fig. 6f).

249 The precipitation dissipates rapidly thereafter and there is almost no precipitation by 0300 LST

250 (Figs. 6g–i). The perturbation wind also weakens quickly and turns to offshore along the northern

251 coast. The magnitude of the perturbation wind is close to zero over the island at 2100 LST (Fig.

252 6g). The land breeze intensifies slowly and nocturnal precipitation initiates along the southeast

253 coast of the island (Fig. 6h). The nocturnal precipitation intensifies to the peak and expands to a

254 larger area at 0300 LST, while the precipitation decreases to a minimum (near zero) over the central

255 island (Fig. 6i).

256   Although the analyses on the precipitation and surface wind observation can efficiently

257 reflect general features of the diurnal rainfall variation and the LSB, they cannot be used to

258 examine the detailed dynamics and thermodynamics processes of the diurnal precipitation cycle

259 and the related LSB over the tropical island. The three-dimensional structures of the LSB, as well

260 as the mechanism of how the LSB triggers and enhances the diurnal precipitation cannot be

261 resolved by the surface observation alone. These aspects were examined using a numerical model,

262 as discussed in the next section.

263

264 **4. Numerical simulation results**

265 **4.1. The simulated diurnal cycle and the influence of the orography**

266   The REAL simulation reproduces the diurnal cycle of precipitation and the associated LSB.

267   The diurnal variations of the 2-meter temperature, 2-meter temperature tendency, and precipitation

268   averaged over the last 26 day of the WRF simulations and all stations over the island (Fig. 7) show

269   generally good agreement with the observations except for slightly higher peak values of simulated

270   2-meter temperature and simulated precipitation (cf. Figs. 7a and 7b). The overall process of the

271   diurnal variation over the island was well simulated, suggesting that the chosen setup of WRF-

272   ARW has the ability to capture the radiative effect due to solar insolation well. The surface

273   temperature begins to increase at 0600 LST and peaks at 1300 LST, coincident with the increase

274   of solar heating. With the rainfall evaporation cooling rate becoming larger than the solar heating

275   rate and/or the radiative cooling later on, the temperature starts to decrease thereafter. After sunset,

276   the temperature drops continuously, reaching its minimum near 0600 LST.

277   The horizontal distribution of precipitation averaged in REAL (Fig. 8a) also has reasonably

278   good agreement with that of the CMORPH data at all hours (Fig. 6a), although the simulated

279   precipitation is slightly larger. The area of heavy precipitation at the center of the island is well

280   captured by the WRF simulation, although the magnitude is noticeably overestimated. The diurnal

281   precipitation cycle is also well revealed by the variation in the horizontal distribution of the

282   simulated precipitation although with a slightly larger magnitude and a 1-hour delay in peak time.

283   The evolution of the simulated surface perturbation wind (on the second lowest model level for

284   horizontal wind, which is the 0.994-sigma level, about 50 meters above the surface) is also

285   consistent with the observation despite some discrepancy in magnitude (Figs. 6 and 8), suggesting

286   that the LSB is well captured as well. However, the evening rainfall along the southern coast is

287   missing, which is likely because the resolution we used in this study was still too coarse to resolve

288 the convection over the southern coast or the physical process was so complex that the model is

289 unable to represent it for now.

290   The results of the NoTER simulation (with removal of island orography) are highly consistent

291 with those of REAL in terms of both the magnitude and timing of each variable averaged over the

292 whole analysis period and at all stations (Figs. 7b and c). Similar results are also found in the

293 horizontal distribution features (Fig. 8 and Fig. 9). Neither the pattern nor the magnitude is altered

294 meaningfully between the two simulations. These results suggest that the diurnal cycle

295 characteristics are not sensitive to the orography over Hainan Island, although many previous

296 studies demonstrated that the orography can play an important role in the precipitation over other

297 islands (Sobel et al. 2011; Hassim et al. 2016; Barthlott and Kirshbaum 2013).

298   In order to simplify the influences of land category and coastline, experiment IDEAL was

299 constructed with an idealized elliptical island to replace the real Hainan Island in the initial

300 condition. The diurnal variation of the 2-meter temperature (blue), 2-meter temperature tendency

301 (red) and hourly accumulated precipitation (green) in IDEAL (Fig. 7d) are nearly identical to those

302 in REAL (Fig. 7b) and the station observation (Fig. 7a) except for their larger magnitudes which

303 could be related to the modified surface land category and the smoothed ellipsoidal coastlines. The

304 diurnal variations of the hourly accumulated precipitation and perturbation wind on the second

305 lowest model level for horizontal wind (Fig. 10) in IDEAL simulation show that the timing of the

306 LSB transitions and the precipitation location are quite similar to those in REAL and the

307 observation with much smoother distribution in the horizontal perturbation wind and precipitation

308 over the island. The relationship between the diurnal variation of precipitation and LSB will be

309 further examined in details based on the results of IDEAL in the next section.

310

4.2. Diurnal variation of precipitation and the related LSB in IDEAL

The mean fields averaged over all hourly model output times during the last 26 days of the simulation depict a southerly low-level prevailing flow over the whole domain, which transports warm moist air to the island from the South China Sea (Fig. 10a). Greater moisture appears in the northern island over the heavy precipitation area under the influence of southwesterly low-to-mid-level flow (850 hPa, Fig. 11a). Higher surface temperature appears over the southern side than that in the northern side (Fig. 12a).

Based on the different phases of surface temperature and perturbation wind, we divided the diurnal cycle process into four stages to elucidate the mechanisms in each stage. The four stages are establishment of a sea breeze (0600–1200 LST), peak sea breeze and peak precipitation (1200–1800 LST), establishment of a land breeze (1800–0000 LST), and peak land breeze phase (0000–0600 LST), respectively. More detailed analyses will be focused on the two middle stages. These are most complicated stages, but are also the most pertinent to the heavy diurnal precipitation (and are therefore most interesting).

a. Stage 1. Establishment of a sea breeze (0600–1200 LST)

This stage commences with the onset of surface heating following sunrise. Because ocean and land have different heat capacities, the island is heated faster than the surrounding ocean. The temperature gradient between the island and the surrounding ocean gradually reverses from offshore to onshore, which results in the weakening and demise of land breeze, and the establishment of a sea breeze over the island.

In early morning hours when the sun is just about to rise, surface air temperatures over the island attain their lowest readings, with air temperatures being a few degrees lower than over the

334   surrounding ocean (Fig. 12b). Owing to persistent solar heating, the surface air temperature over

335   most part of the island exceeds the ocean by 0900 LST (Fig. 12c). Meanwhile, the surface air

336   temperature gradient is directed from offshore to onshore, although the land breeze still persists

337   over the island at this time.

338   The local rate of warming is inhomogeneous over the island. The surface temperature in the

339   northeastern part of the island are considerably lower than that in other regions where the

340   temperatures surpass the surrounding ocean by 0900 LST. The slower warming in the northeastern

341   part of the Hainan Island is likely due to the morning fog or cold pool air (Fig. 13b) that commonly

342   forms within the area humidified (Fig. 14b) by late-afternoon precipitation on the preceding day.

343   The cloud over the area attenuates solar radiation and subsequently slows the local warming.

344   Moreover, positive horizontal temperature advection exists over the southern island (Fig. 15a and

345   b), which helps to increase the temperature faster over the area. The sea breeze begins to develop

346   along the southwestern coastline owing to the weakest land breeze and the highest warming rate,

347   while other areas of the island are still under the control of the land breeze with an offshore

348   temperature gradient (Fig. 12c). Two land breeze circulations (LBCs) appear clearly in the vertical

349   direction below 3 km along the coast of the island at 0600 LST (Fig. 14b). The southern LBC

350   recedes quickly with the reversal of the temperature gradient at around 0900 LST, while the other

351   LBC remains distinct (Fig. 14c).

352   By 1200 LST, the temperature gradient reverses to the onshore direction, while the sea breeze

353   has fully established along the entire coastal line (Fig. 12d). Unevenly warming speeds over the

354   island with much more rapid warming over the north while slower warming over the south, which

355   is a result of a high negative horizontal temperature advection over the southern island along the

356   coastlines (Fig. 15d). A sea-breeze front appears at the leading edge of the sea breeze along the

357   coastline, particularly along the northernmost coast where the maximum near-surface temperature

358   gradient lies (Fig. 12d). At the same time, copious water vapor is transported inland from the ocean

359   owing to the low-to-mid level prevailing wind (Fig. 11d) and upward motions (Fig. 14d). Clouds

360   initially form along the sea-breeze (Fig. 13c) and subsequently produces rainfall (shaded in Fig.

361   10d and green lines in Fig. 13d). Noticeably, more rapid warming during this period happens over

362   the northwest of the island while it is much slower over the other areas (Fig. 12d), which is because

363   of the horizontal gradient and advection of the temperature over the whole island (Fig. 15).

364

365   **b. Stage 2. Peak sea breeze and peak precipitation (1200−1800 LST)**

366   Surface temperature is a maximum from 1200 to 1400 LST over most of the island, then

367   decreases rapidly thereafter owning primarily to the development of precipitation (which has its

368   diurnal maximum during this period) and associated evaporative cooling. Besides, surface

369   temperature is also controlled by other processes, such as surface heat fluxes, both shortwave and

370   long wave radiative processes, diffusion in the soil, etc. The sea breeze also reaches its peak

371   intensify in the 1200-1400 LST time period.

372   At 1500 LST, surface temperature decreases over the rainfall area owing to evaporation

373   cooling and slightly increases over other areas because of continuous solar heating (Fig. 12e).

374   There is significant enhancement in upward motions in the low to middle troposphere (Fig. 14e).

375   The sea breeze reaches its peak strength and greatest inland penetration (Fig. 12e). Two distinct

376   sea breeze circulations (SBCs) are clearly seen in the vertical cross section, with the stronger one

377   over the northern flank of the island (Fig. 14e). Moisture air is transported from ocean to the island

378   persistently by the deep southwesterly prevailing wind throughout the lower troposphere (Fig. 11e)

379   while low-level convergence of moisture air generating strong updraughts, which results in an

380   increase of the moisture over the midlevels (Fig.14e). These factors favor the development of deep

381   convection over the northern flank of the island. As a result, precipitation increases significantly

382   along the sea breeze front (Fig. 10e).

383   By 1800 LST, the strongest rainfall falls over the island (Fig. 10f) owning to strongest low-

384   level convergence and subsequent lifting of warm moist air (Fig. 14f). The sea breeze fronts move

385   further inland and collide with each other near the center of the island (Fig. 12f), with a deep layer

386   of moisture over the northern side of the island that fuels the strong precipitation (Figs. 11f and

387   14f). Cold pools form due to the evaporation cooling of the precipitation, contributing to the

388   propagation and enhancement of the precipitation, which will be further examined with two other

389   sensitivity experiments in the next part. The precipitation pattern (Fig. 10f) exhibits a horseshoe

390   shape aligned with the prevailing wind direction, which is similar to the result of the urban heat

391   island study by Han and Baik (2008).

392

393   **c. Stage 3. Establishment of a land breeze (1800–0000 LST)**

394   During this period, the convection quickly dissipates and the sea breeze is replaced by a land

395   breeze (Figs. 10g and h) after sunset. The surface temperature decreases continuously throughout

396   this stage over the island. The rate of temperature decrease is fastest in the first several hours,

397   reaching around -1.5 K h^{-1} at 1800-1900 LST (red line in Fig. 7d) due to the sudden loss of solar

398   heating. The horizontal temperature gradient begins to reverse, which eventually leads to the

399   establishment of the land breeze (Figs. 12g and h). By 2100 LST, approximately two hours after

400   sunset, temperature over the island is decreasing rapidly both at the surface (Fig. 12g) and

401   throughout the boundary layer. Meanwhile, subsidence becomes dominant over the island (Fig.

402 14g). The subsidence dries the lower levels and rainfall has ceased over the whole island (Fig.

403 13g).

404 By 0000 LST, with the continuous decreasing of temperature and amplifying of the offshore

405 temperature gradient, the land breeze circulations are well established in particular across the shore

406 of the northern island (Fig. 14h). Further drying is seen in mid-to-low levels as the much stronger

407 downward flow occurs over the island, which transports dry air from aloft to the mid-to-low levels

408 (Figs. 11h and 14h). At the same time, under the influence of the prevailing wind, much more

409 moisture air is concentrated over the northern island, so the moisture over the northern island is

410 much moister than the southern island. Clouds vanish quickly and precipitation dissipates almost

411 completely by this time.

412

413 **d. Stage 4. Peak land breeze (0000−0600 LST)**

414 The land breeze reaches its maximum intensity during this period. Nighttime radiative cooling

415 results in the minimum temperature being attained at approximately 0500 LST. From 0000 to 0300

416 LST, the land breeze intensifies rapidly along the northwest coast, becoming nearly perpendicular

417 to the coastline and parallel with the low-level prevailing wind as the surface temperature over

418 land decreases (Fig. 12i). Two LBCs are evident in the vertical cross section (Fig. 13i). Subsidence

419 extends over the entire island (Fig. 14i). The peak land breeze is established at 0600 LST (Fig.

420 12b). The strong subsidence also leads to further midlevel drying (Fig. 11b). Near the surface, the

421 cooling is associated with an increase in the relative humidity, which induces the formation of low

422 clouds and fog (Fig. 13b).

423

424 **4.3. The impacts of latent heating/cooling on LSB and the related rainfall**

425   Surface temperature in the FakeDry experiment agrees well with the IDEAL over the island,

426   which indicates that the solar heating rather than the latent heating/cooling is primarily responsible

427   for the temperature variability. Although the precipitation is decreased significantly, light rainfall

428   still occurs in the late afternoon in conjunction with the sea breeze front, but with an approximate

429   3-h delay in convective initiation. The precipitation attains its maximum at 1800 LST, which along

430   with the peak sea breeze, also lags that in the IDEAL experiment by approximately three hours.

431   The impact of cold pool and latent cooling on the sea breeze and rainfall was further examined

432   using the Hovmöller diagrams of zonal wind perturbations on the second lowest model level for

433   horizontal wind and hourly precipitation along the red line in Fig. 1 for experiments IDEAL,

434   FakeDry and NOVAP (Fig. 16). A weaker sea breeze is observed in the FakeDry experiment than

435   in the IDEAL experiment while NOVAP experiment shows the strongest sea breeze. The NOVAP

436   experiment generated much stronger precipitation over the island as the rain evaporation cooling

437   process was turned off. The propagation of the LSB is much slower and the inland propagation

438   distance is much shorter in FakeDry experiment than that in the IDEAL experiment while the

439   propagation speed in NOVAP experiment is between the other two experiments, which suggests

440   that cold pool can accelerate the precipitation over the tropical island. In the NOVAP experiment,

441   the heavy precipitation does not dissipate after 2100 LST but propagates into the northeast out of

442   the island with the land breeze, indicating that cold pool plays an important role in dissipating the

443   convection. Moreover, given precipitation varies precisely with the convergence and divergence

444   of horizontal winds due to LSB in all simulations, it is evident that the LSB is the primarily forcing

445   for the diurnal precipitation variability over the island.

446   The LSB circulations in the FakeDry experiment are similar to those in the IDEAL experiment,

447   even consistent with NOVAP experiment, except that they are confined to lower levels (around 2

448   km) owing to weaker vertical motion (Strong vertical velocity can extend over 5 km in IDEAL

449   experiment, while it can only reach 2 km in FakeDry experiment. Figures omitted). The latent

450   heating can strengthen vertical movement and extend the LSB circulations to higher altitudes. The

451   latent heating feedback can also lead to stronger and earlier convection initiation and precipitation

452   along the sea breeze fronts. In turn, the cold pool further promotes the inland penetration of the

453   sea-breeze front and dissipates the precipitation (Fig. 16), which is because the pressure gradient

454   increases and drives the sea breeze flow more inland when cold pool moves toward the

455   island/inland.

456

5. Summary

458   Diurnal cycle of precipitation over tropical area is poorly captured by numerical models,

459   owing to model uncertainties in depicting the physical mechanisms that underlie the diurnal

460   precipitation cycle, which is considered to be closely linked with the land-sea breeze. This study

461   explored the diurnal precipitation variation and its relationship with the land/sea breeze

462   circulations on Hainan Island, a tropical island located off the southern coast of China, based on

463   gauge observation and satellite-estimated precipitation, as well as convection-permitting

464   numerical simulations. The diurnal cycle of precipitation in each month over the island was

465   analyzed with 19 gauge observations during 1951–2010. Most precipitation fall during warm

466   season (from April to October) and exhibit a significant diurnal cycle, whereas much lesser

467   precipitation fall in other months. Precipitation is a maximum between 1500–1700 LST in the

468   warm season at almost all stations except for four stations along the southern coastline of the island.

469   The satellite-derived CMORPH precipitation estimates from 2006–2015 were further used to

470   validate the diurnal precipitation variation. The CMORPH data agrees well with gauge observation

471 except for a smaller magnitude of precipitation and a 1-hour delay in the timing of the daily

472 precipitation maximum during the warm season. The analyses on CMORPH data show that about

473 60% of the total annual precipitation over the island is attributable to diurnal variations, with the

474 largest proportion in May and the smallest proportion in September and October. For May and

475 June, precipitation begins around local noon time, intensifying quickly thereafter, and reaching a

476 peak at ~1500 LST based on station observations. This diurnal rainfall cycle is, for the most part

477 consistent with the diurnally varying low-level wind convergence and divergence.

478   A series of numerical simulations (REAL, NoTER, IDEAL, FakeDry and NOVAP) using a

479 convection-permitting configuration of the WRF model (2-km horizontal grid spacing) were

480 conducted to understand the underlying mechanisms of the diurnal precipitation variations. The

481 initial and cyclic lateral boundary conditions were generated using a 10-year (2006–2015) average

482 of ERA-interim data for May and June. Results show that the orography of Hainan Island may be

483 of only secondary influence on the diurnal precipitation cycle, which is different from past studies

484 on other hilly islands. Similar diurnal cycles of precipitation and related land/sea breeze

485 circulations were simulated between simulations with and without orography over the island. Even

486 with an idealized island, which is an elliptical flat island located at the same place with similar

487 area and orientation, but only grassland land cover, the diurnal cycle characteristics can still be

488 fairly well captured. Those results show that: (1) WRF is capable of replicating the important

489 aspects of the mean diurnal cycle compared to rainfall observations, (2) removing the orography

490 and coastal features made little difference to the diurnal cycle during the rainiest times of the year,

491 (3) the dominant process that produces the diurnal cycle were shown to be the sea/land breezes

492 caused by the relative surface heating/cooling of the island compared to the surrounding ocean,

493   and (4) evaporative cooling as part of convective systems also plays an important role in the

494   diurnal cycle.

495   The simulated diurnal cycle of precipitation and related land/sea breeze circulations based on

496   the idealized flat-island simulation were divided into four stages in terms of the evolutions of

497   temperature, winds and precipitation. Stage 1 is from 0600 to 1200 LST, during which time the

498   land breeze is replaced by a sea breeze as solar heating warms the interior of the island. Abundant

499   moisture is transported to the low to middle troposphere over the island, resulting in convective

500   initiation and precipitation along the sea-breeze front. Stage 2 is from 1200 to 1800 LST, during

501   which time sea breeze attains to its peak intensity and precipitation is a maximum. The sea breezes

502   from opposite sides of the island eventually penetrate all the way to the island's center and collide,

503   which results in the maximum precipitation being located there. Stage 3 is from 1800 to 0000 LST,

504   during which time a land breeze is established as a result the cooling over the island. The cooling

505   is due primarily to the sudden loss of solar heating. Subsidence from the land breeze prevents

506   further precipitation by early evening. The last stage covers the peak of the land breeze, which is

507   observed near sunrise.

508   The FakeDry and NOVAP experiments show that the latent cooling and cold pool have a small

509   impact on the land/sea breeze circulations but can apparently enhance precipitation. Strong

510   convection can enhance the sea breeze, and the augmentation of the sea breeze by the evaporatively

511   driven cold pool helps to accelerate the inland propagation of the sea breeze and weakens the

512   convection.

513   Finally, it is worth mentioning that the 1-hour delay in the timing of the maximum

514   precipitation in the simulation is probably caused by the 2-km horizontal resolution, which may

515   not be high enough to resolve explicit underlying physical processes. It is likely for the same reason

516   that the weak nocturnal precipitation is not captured by the simulations. Much higher horizontal

517   and vertical resolution might be needed in the future work to resolve more detailed processes

518   related to the diurnal cycles. On the other hand, there are many other factors like biases in ERA-

519   Interim reanalysis data used for the initial and boundary conditions to drive the numerical

520   simulations and biases in physical processes (microphysics, surface processes, radiative process,

521   etc), which will be studied in follow-on work. Moreover, the rainfall for different seasons shows

522   quite different patterns, owing to various underlying dynamic and thermodynamic physics. In

523   addition to May and June that were mainly examined in this current work, the diurnal rainfall

524   variation in other months needs to be explored in further studies.

525

526   **Acknowledgments:** Lei Zhu is supported by the Natural Science Foundation of China Grant

527   41461164006, and the Chinese Scholarship Council (CSC). Zhiyong Meng is supported by the

528   Natural Science Foundation of China Grants 41461164006, 41425018 and 41375048. Fuqing

529   Zhang is supported by the Office of Naval Research Grant N000140910526 and the National

530   Science Foundation Grant AGS-1305798. Paul Markowski is supported by National Science

531   Foundation grant AGS-1536460 and National Oceanic and Atmospheric Administration awards

532   NA15NWS4680012 and NA14NWS4680015. The simulations were performed on the Stampede

533   supercomputer of the Texas Advanced Computing Center (TACC). All data are freely available

534   from sources indicated in the text or from the corresponding author upon request (Email:

535   zymeng@pku.edu.cn).

536   **References**

537   Bao, X., Zhang, F. and Sun, J., 2011. Diurnal variations of warm-season precipitation east of the
538   Tibetan Plateau over China. *Monthly Weather Review*, *139*(9), pp.2790–2810.
539
540   Bao, X. and Zhang, F., 2013. Impacts of the mountain-plains solenoid and cold pool dynamics on
541   the diurnal variation of warm-season precipitation over northern China. *Atmos. Chem. Phys*, *13*,
542   pp.6965–6982.
543
544   Barthlott, C., and D. J. Kirshbaum, 2013: Sensitivity of deep convection to terrain forcing over
545   Mediterranean islands. *Q. J. R. Meteorol. Soc.*, *139*, pp.1762–1779.
546
547   Chen, X., Zhang, F. and Zhao, K., 2016. Diurnal Variations of the Land–Sea Breeze and Its
548   Related Precipitation over South China. *Journal of the Atmospheric Sciences*, *73*(12), pp.4793–
549   4815.
550
551   Chen, X., Zhang, F. and Zhao, K., 2017. Influence of Monsoonal Wind Speed and Moisture
552   Content on Intensity and Diurnal Variations of the Mei-yu Season Coastal Rainfall over South
553   China. *Journal of the Atmospheric Sciences*, *in review*.
554
555   Crosman, E.T. and Horel, J.D., 2010. Sea and lake breezes: a review of numerical
556   studies. *Boundary-layer meteorology*, *137*(1), pp.1–29.
557
558   Dai, A., 2001. Global precipitation and thunderstorm frequencies. Part I: Seasonal and interannual
559   variations. *Journal of climate*, *14*(6), pp.1092-1111.
560
561   Dee, D.P., Uppala, S.M., Simmons, A.J., Berrisford, P., Poli, P., Kobayashi, S., Andrae, U.,
562   Balmaseda, M.A., Balsamo, G., Bauer, P. and Bechtold, P., 2011. The ERA-Interim reanalysis:
563   Configuration and performance of the data assimilation system. *Quarterly Journal of the royal*
564   *meteorological society*, *137*(656), pp.553–597.
565
566   Dudhia, J., 1989. Numerical study of convection observed during the winter monsoon experiment
567   using a mesoscale two-dimensional model. *Journal of the Atmospheric Sciences*, *46*(20), pp.3077-
568   3107.
569
570   Han, J.Y. and Baik, J.J., 2008. A theoretical and numerical study of urban heat island–induced
571   circulation and convection. *Journal of the Atmospheric Sciences*, *65*(6), pp.1859–1877.
572
573   Hassim, M.E.E., Lane, T.P. and Grabowski, W.W., 2016. The diurnal cycle of rainfall over New
574   Guinea in convection-permitting WRF simulations. *Atmos. Chem. Phys*, *16*(1), pp.161–175.
575
576   He, H. and Zhang, F., 2010. Diurnal variations of warm-season precipitation over northern
577   China. *Monthly Weather Review*, *138*(4), pp.1017–1025.
578

579 Hong, S.Y., Dudhia, J. and Chen, S.H., 2004. A revised approach to ice microphysical processes
580 for the bulk parameterization of clouds and precipitation. *Monthly Weather Review*, *132*(1),
581 pp.103–120.

583 Hong, S.Y., Noh, Y. and Dudhia, J., 2006. A new vertical diffusion package with an explicit
584 treatment of entrainment processes. *Monthly Weather Review*, *134*(9), pp.2318–2341.

586 Huffman, G.J., Bolvin, D.T., Nelkin, E.J., Wolff, D.B., Adler, R.F., Gu, G., Hong, Y., Bowman,
587 K.P. and Stocker, E.F., 2007. The TRMM multisatellite precipitation analysis (TMPA): Quasi-
588 global, multiyear, combined-sensor precipitation estimates at fine scales. *Journal of
589 Hydrometeorology*, *8*(1), pp.38–55.

591 Iacono, M.J., Delamere, J.S., Mlawer, E.J., Shephard, M.W., Clough, S.A. and Collins, W.D., 2008.
592 Radiative forcing by long-lived greenhouse gases: Calculations with the AER radiative transfer
593 models. *Journal of Geophysical Research: Atmospheres*, *113*(D13).

595 Joyce, R.J., Janowiak, J.E., Arkin, P.A. and Xie, P., 2004. CMORPH: A method that produces
596 global precipitation estimates from passive microwave and infrared data at high spatial and
597 temporal resolution. *Journal of Hydrometeorology*, *5*(3), pp.487–503.

599 Keenan, T.D., Holland, G.J., Manton, M.J. and Simpson, J., 1988. TRMM ground truth in a
600 monsoon environment: Darwin, Australia. *Australian Meteorological Magazine*, *36*(2), p.81.

602 Kishtawal, C.M. and Krishnamurti, T.N., 2001. Diurnal variation of summer rainfall over Taiwan
603 and its detection using TRMM observations. *Journal of Applied Meteorology*, *40*(3), pp.331-344.

605 Liang, Z. and Wang, D., 2016. Sea breeze and precipitation over Hainan Island. *Quarterly Journal
606 of the Royal Meteorological Society*.

608 Mapes, B.E., Warner, T.T. and Xu, M., 2003. Diurnal patterns of rainfall in northwestern South
609 America. Part III: Diurnal gravity waves and nocturnal convection offshore. *Monthly Weather
610 Review*, *131*(5), pp.830–844.

612 Neale, R. and Slingo, J., 2003. The maritime continent and its role in the global climate: A GCM
613 study. *Journal of Climate*, *16*(5), pp.834–848.

615 Nguyen, H., Protat, A., Kumar, V., Rauniyar, S., Whimpey, M. and Rikus, L., 2015. A regional
616 forecast model evaluation of statistical rainfall properties using the CPOL radar observations in
617 different precipitation regimes over Darwin, Australia. *Quarterly Journal of the Royal
618 Meteorological Society*, *141*(691), pp.2337–2349.

620 Ogino, S.Y., Yamanaka, M.D., Mori, S. and Matsumoto, J., 2016. How Much is the Precipitation
621 Amount over the Tropical Coastal Region?. *Journal of Climate*, *29*(3), pp.1231–1236.

623 Qian, J.H., 2008. Why precipitation is mostly concentrated over islands in the Maritime
624 Continent. *Journal of the Atmospheric Sciences*, *65*(4), pp.1428–1441.

Skamarock, W.C., Klemp, J.B., Dudhia, J., Gill, D.O., Barker, D.M., Duda, M.G., Huang, X.Y., Wang, W. and Jordan, G., *Powers. 2008. A Description of the Advanced Research WRF Version 3. NCAR Technical Note*. NCAR/TN–475+ STR.

Sobel, A.H., Burleyson, C.D. and Yuter, S.E., 2011. Rain on small tropical islands. *Journal of Geophysical Research: Atmospheres*, *116*(D8).

Sun, J. and Zhang, F., 2012. Impacts of mountain–plains solenoid on diurnal variations of rainfalls along the mei-yu front over the east China plains. *Monthly Weather Review*, *140*(2), pp.379–397.

Trier, S.B., Davis, C.A. and Ahijevych, D.A., 2010. Environmental controls on the simulated diurnal cycle of warm-season precipitation in the continental United States. *Journal of the Atmospheric Sciences*, *67*(4), pp.1066–1090.

Tu, X., Zhou, M.Y., Z. and Sheng, S.H., 1993. The mesoscale numerical simulation of the flow field of the Hainan Island and the Leizhou Peninsula. *Acta Oceanolog (in Chinese)*, *12*(2), pp.219–235.

Wapler, K. and Lane, T.P., 2012. A case of offshore convective initiation by interacting land breezes near Darwin, Australia. *Meteorology and Atmospheric Physics*, *115*(3–4), pp.123–137.

Yang, G.Y. and Slingo, J., 2001. The diurnal cycle in the tropics. *Monthly Weather Review*, *129*(4), pp.784–801.

Zhai, W., Li, G., Sun, B. and Dang, R., 1998. Varying season's mesoscale wind field circulation in Hainan island. J. Trop. Meteorol. 4: 79–87.

Zhang, Y., Zhang, F. and Sun, J., 2014. Comparison of the diurnal variations of warm-season precipitation for East Asia vs. North America downstream of the Tibetan Plateau vs. the Rocky Mountains. *Atmospheric Chemistry and Physics*, *14*(19), pp.10741–10759.

 Figure Captions

659

660 FIG. 1. Configuration of model domain, gauge-based station points (color dots correspond to the
661 time series shown in Fig. 2) over Hainan Island and the terrain height (shading, m). The red ellipse
662 is the idealized representation of the island (used for the idealized simulations), and the red vertical
663 line indicates the location of the vertical cross-sections shown in Figs. 14 and 16.

664

665 FIG. 2. Average rainfall accumulations by hour, each month of the year, obtained from the rain
666 gauge network. The color is consistent with the color dots over the island in Fig. 1. LST means the
667 Local Standard Time.

668

669 FIG. 3. Average station rainfall accumulations obtained from gauges (blue) and CMORPH (red)
670 in each month.

671

672 FIG. 4. Fraction of the total precipitation that can be attributed to the diurnal cycle, by month
673 (shading), along with average hourly precipitation accumulations (black contours every 0.05 mm,
674 starting at 0.25 mm).

675

676 FIG. 5. Average rainfall accumulations by hour in May and June (a) from rain gauges and (b)
677 derived from CMORPH.

678

679 FIG. 6. Ten-year average, hourly rainfall accumulations at 3-h intervals for May and June derived
680 from CMORPH (shading) except used 1700 LST as it is the strongest rainfall time in CMORPH
681 observation. Three-year average wind velocity (vectors) is also shown. Rain gauge locations are
682 indicated in (a).

683

684 FIG. 7. The average of 2-meter temperature (T2_avg), 2-meter temperature tendency
685 (T2_tendency, temperature difference between two neighboring hours), and hourly rainfall
686 accumulation over the island based on (a) gauge observations, (b) simulation REAL, (c) simulation
687 NoTER, (d) and simulation IDEAL. Horizontal colored lines indicate means over all hours.

688

689 FIG. 8. Hourly precipitation accumulation (shading) and average perturbation wind (vectors) on
690 the second lowest model level for horizontal wind in simulation REAL every 3 h. The averages
691 over all hours are shown in (a).

692

693 FIG. 9. As in FIG. 8, but for simulation NoTER.

694

695 FIG. 10. As in FIG. 8, but for simulation IDEAL.

696

697 FIG. 11. Water vapor mixing ratio (shading) and horizontal wind (vectors) at 850 hPa, and hourly
698 precipitation accumulations > 0.1 mm (thick purple contours), (b–i) every 3 h and (a) averaged
699 over all times.

700

701 FIG. 12. (a) 2-meter mean temperature (shading) and horizontal wind (vectors) on the second
702 lowest model level for horizontal wind; (b–i) 2-meter mean temperature perturbation (shading)

703 and mean perturbation horizontal wind (vectors) on the second lowest model level every 3 h. The
704 right color bar is used for (a).

705

706 FIG. 13. Cloud water mixing ratio (red shading), 2-meter temperature (grey shaded), perturbation
707 horizontal wind on the second lowest model level for horizontal wind (yellow vectors), and hourly
708 precipitation accumulation (green contour lines) every 3 h.

709

710 FIG. 14. Vertical cross-sections of relative humidity (shading), perturbation wind (vectors; the
711 scale of the vertical component is increased by a factor of 5), and temperature (contours) in the
712 south-to-north direction (see red line in Fig. 1) averaged over all hours (a) and at 3-h intervals (b–
713 i). The triangles in each panel indicate the edges of the island.

714

715 FIG. 15. Horizontal temperature advection (shaded) and horizontal wind (vector, m s^{-1}) on the
716 first model level in simulation IDEAL.

717

718 FIG. 16. Hovmoller diagrams of perturbation meridional wind component on the second lowest
719 model level for horizontal wind (shading) in the (a) IDEAL, (b) Fakedry and (c) NOVAP
720 simulations, respectively. Precipitation exceeding 0.1 mm h^{-1} is enclosed by the heavy purple
721 contours. The two vertical dash lines indicate the edges of the island.

722
723
724
725
726
727
728
729
730
731
732
733

734

Table 1

Station observation period used over Hainan Island

Station No.	Latitude	Longitude	Height (m)	Obs period(YearMonth)	Name
59757	20	110.37	9.9	197701-201212	Qiongshan
59758	20	110.25	63.5	195101-201212	Haikou
59838	19.1	108.62	7.6	195506-201212	Dongfang
59842	19.9	109.68	31	196201-201212	Lingao
59843	19.73	110	31.4	195901-201212	Dengmai
59845	19.52	109.58	169	195505-201212	Zanzhou
59847	19.27	109.05	98.1	196605-201212	Changjiang
59848	19.23	109.43	215.6	196201-201212	Baisha
59849	19.03	109.83	250.9	195602-201212	Qiongzhong
59851	19.7	110.33	24.2	196301-201212	Dingan
59854	19.37	110.1	118.3	196301-201212	Tunchang
59855	19.23	110.47	24	195509-201212	Qiaonghai
59856	19.62	110.75	21.7	195901-201212	Wenchang
59940	18.75	109.17	155	196202-201212	Ledong
59941	18.77	109.52	328.5	196301-201212	Wuzhishan
59945	18.65	109.7	68.6	196509-201212	Baoting
59948	18.22	109.58	419.4	196201-201212	Sanya
59951	18.8	110.33	39.9	196201-201212	Wanning
59954	18.5	110.03	13.9	195601-201212	Lingshui

750 **Figures**
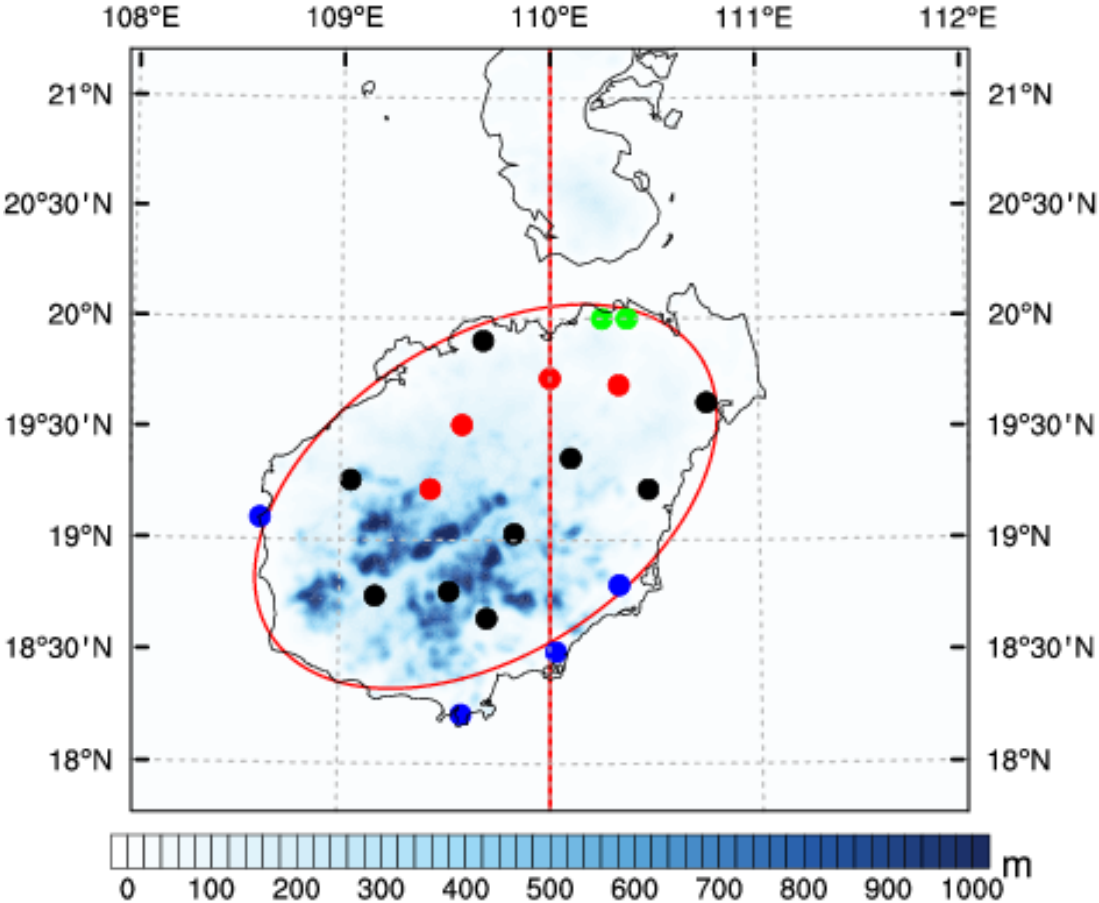
751
752
753

754
755 FIG. 1. Configuration of model domain, gauge-based station points (color dots correspond to the
756 time series shown in Fig. 2) over Hainan Island and the terrain height (shading, m). The red ellipse
757 is the idealized representation of the island (used for the idealized simulations), and the red vertical
758 line indicates the location of the vertical cross-sections shown in Figs. 14 and 16.
759
760
761
762
763
764
765
766
767
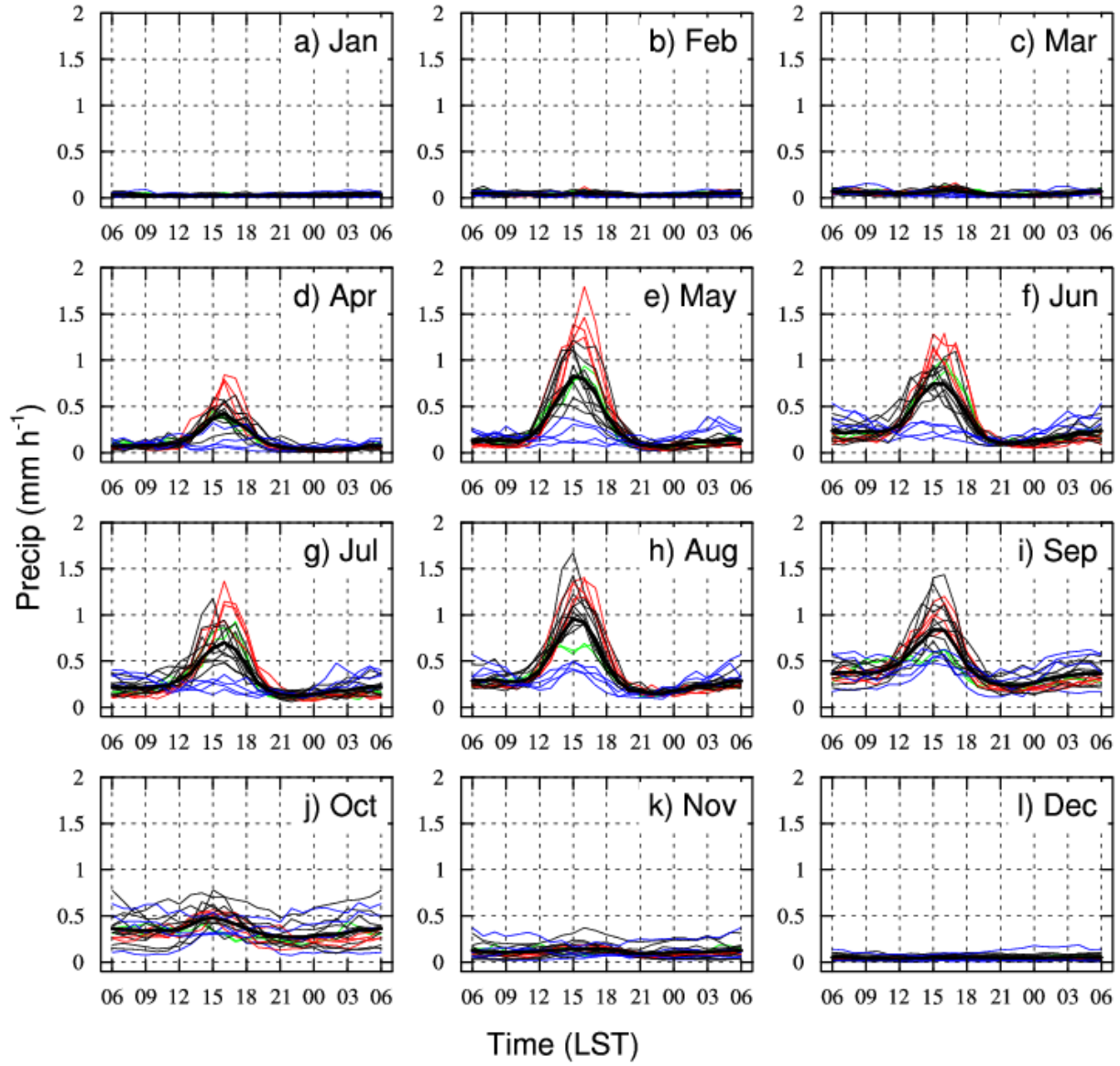
FIG. 2. Average rainfall accumulations by hour, each month of the year, obtained from the rain gauge network. The color is consistent with the color dots over the island in Fig. 1. LST means the Local Standard Time.
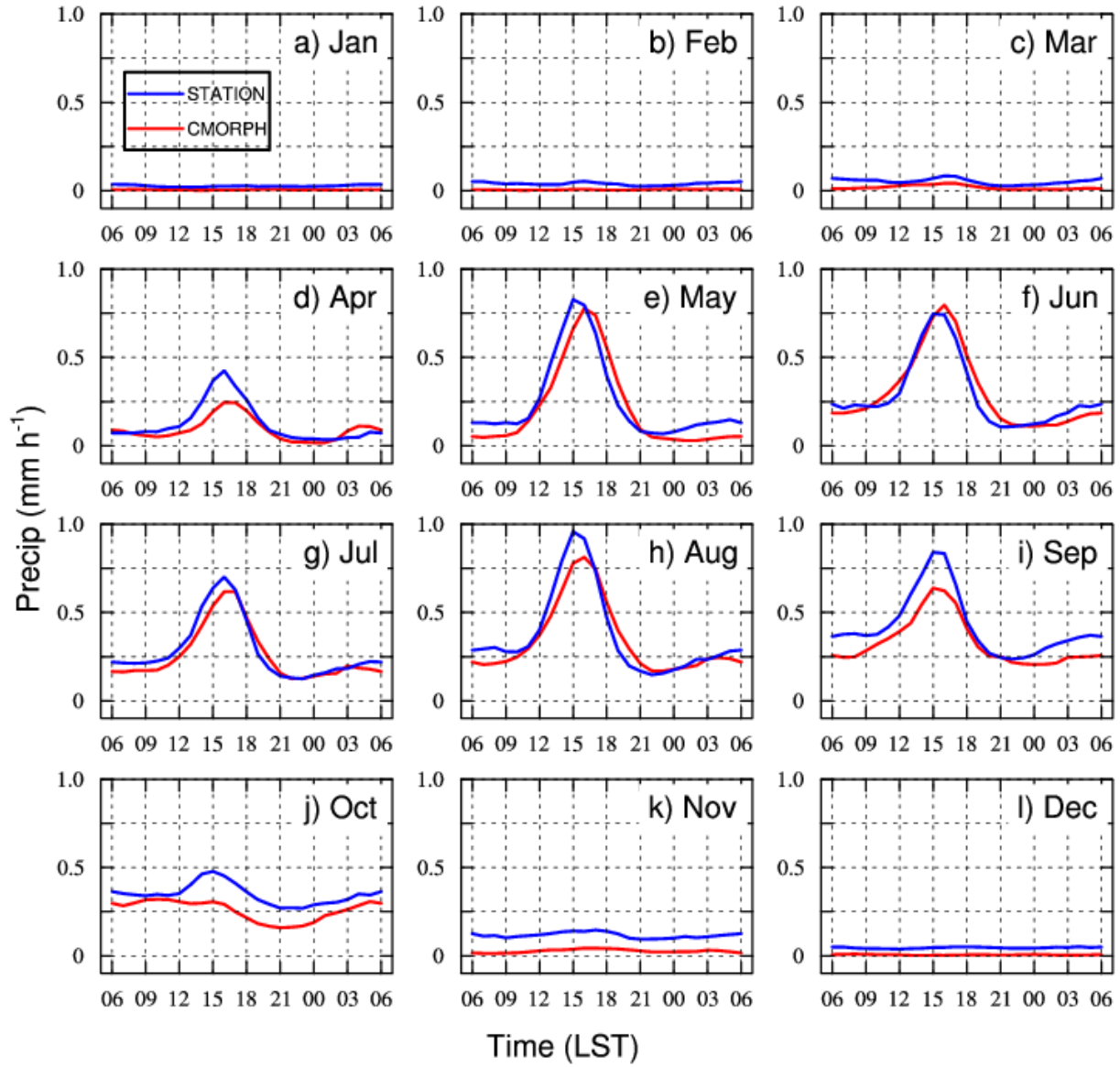
782
783
784 FIG. 3. Diurnal cycles of hourly average rainfall accumulations obtained from gauges (blue) and
785 CMORPH (red) in each month.
786
787
788
789
790
791
792
793
794
795
796

797
798
799 FIG. 4. Fraction of the total precipitation that can be attributed to the diurnal cycle, by month
800 (shading), along with average hourly precipitation accumulations (black contours every 0.05 mm
801 h^{-1}, starting at 0.25 mm h^{-1}).
802
803
804
805
806
807
808
809
810
811

812
813
814
815
816
817
818

819
820
821 FIG. 5. Average rainfall accumulations by hour in May and June (a) from rain gauges and (b)
822 derived from CMORPH.
823
824
825
826
827
828
829
830
831
832
833
834
835
836
837
838
839
840
841
842
843
844
845
846

847
848
849 FIG. 6. Ten-year average, hourly rainfall accumulations at 3-h intervals for May and June derived
850 from CMORPH (shading) except used 1700 LST as it is the strongest rainfall time in CMORPH
851 observation. Three-year average wind velocity (vectors) is also shown. Rain gauge locations are
852 indicated in (a).
853
854
855
856
857
858
859
860
861
862
863
864
865
866
867
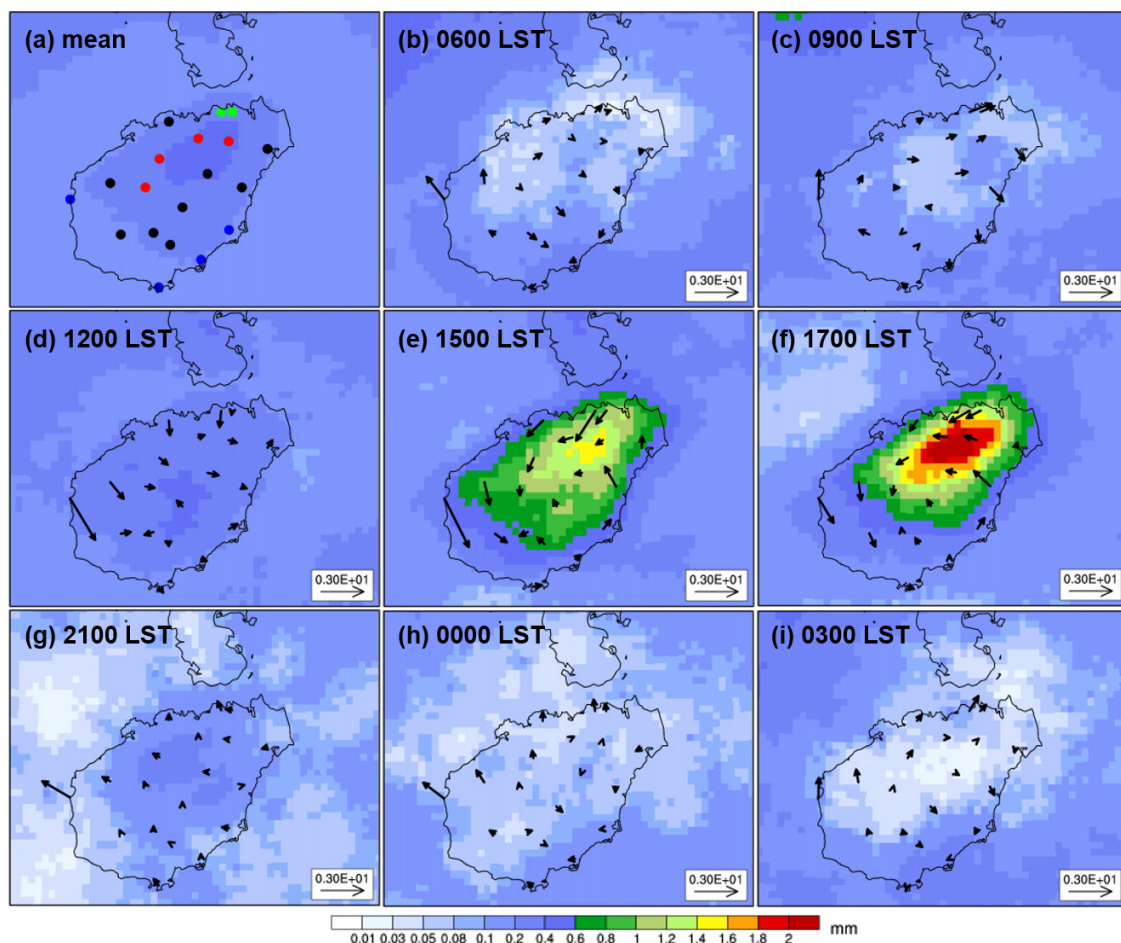
FIG. 7. The average of 2-meter temperature (T2_avg), 2-meter temperature tendency (T2_tendency, temperature difference between two neighboring hours), and hourly rainfall accumulation over the island based on (a) gauge observations, (b) simulation REAL, (c) simulation NoTER, (d) and simulation IDEAL.

898
899

900
901
902 FIG. 8. Hourly precipitation accumulation (shading) and average perturbation wind (vectors) on
903 the second lowest model level for horizontal wind in simulation REAL every 3 h. The averages
904 over all hours are shown in (a).
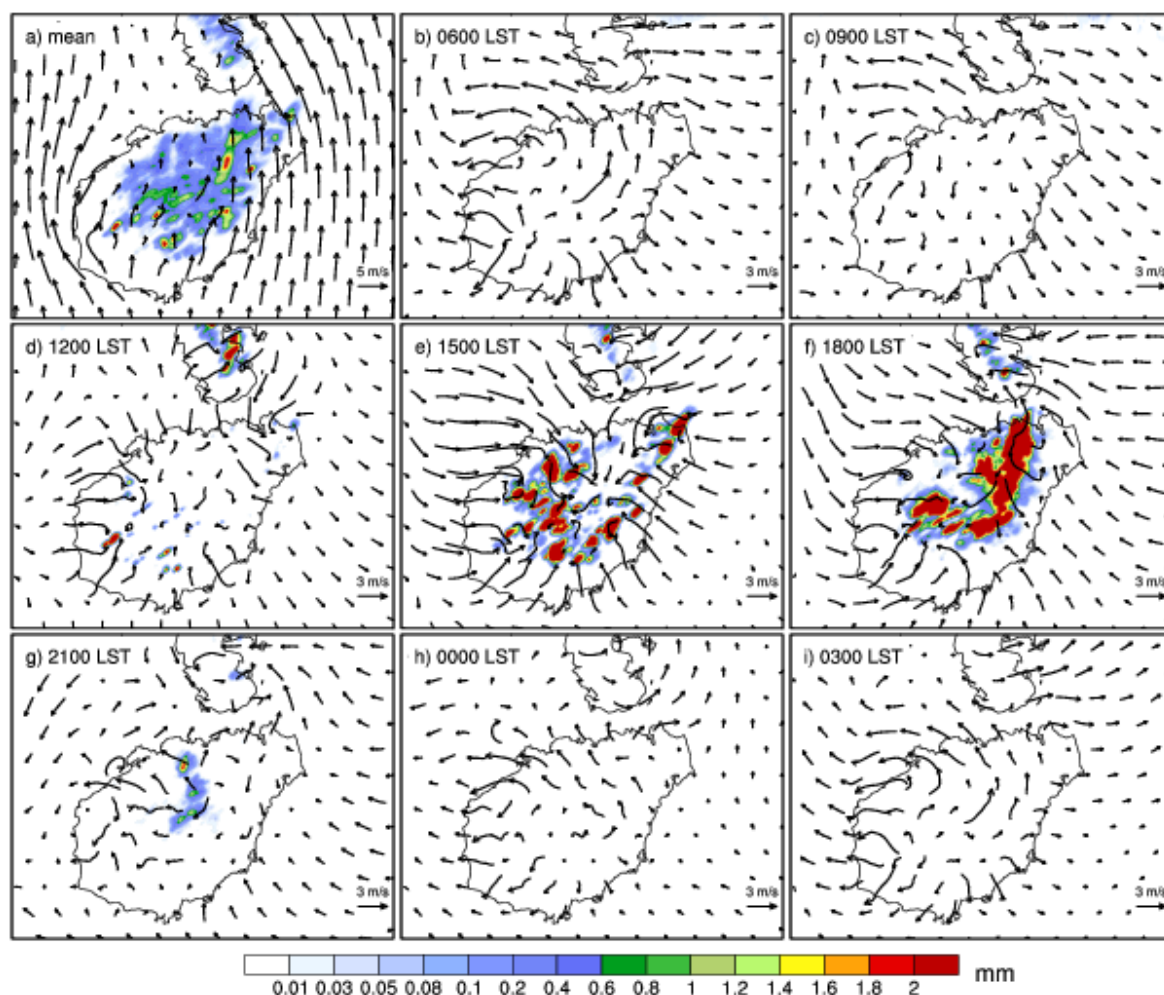
905
906
907
908
909
910
911
912
913
914
915
916
917

918

919
920
921   FIG. 9. As in FIG. 8, but for simulation NoTER.
922
923
924

925
926
927 FIG. 10. As in FIG. 8, but for simulation IDEAL.
928
929
930
931
932
933
934
935
936
937
938
939
940
941
942
943
944

945
946

947
948
949 FIG. 11. Water vapor mixing ratio (shading) and horizontal wind (vectors) at 850 hPa, and hourly
950 precipitation accumulations > 0.1 mm (thick purple contours), (b–i) every 3 h and (a) averaged
951 over all times in IDEAL simulation.
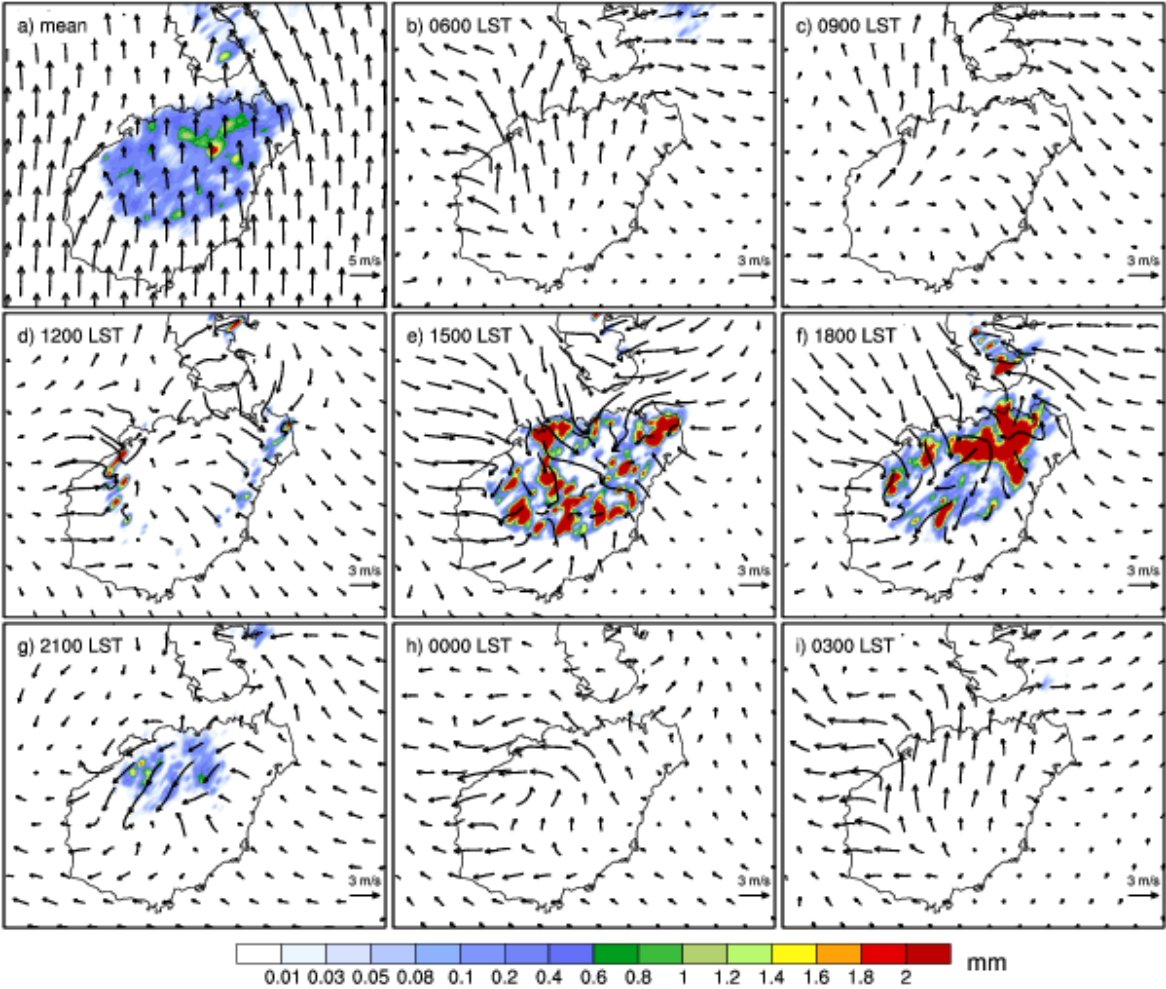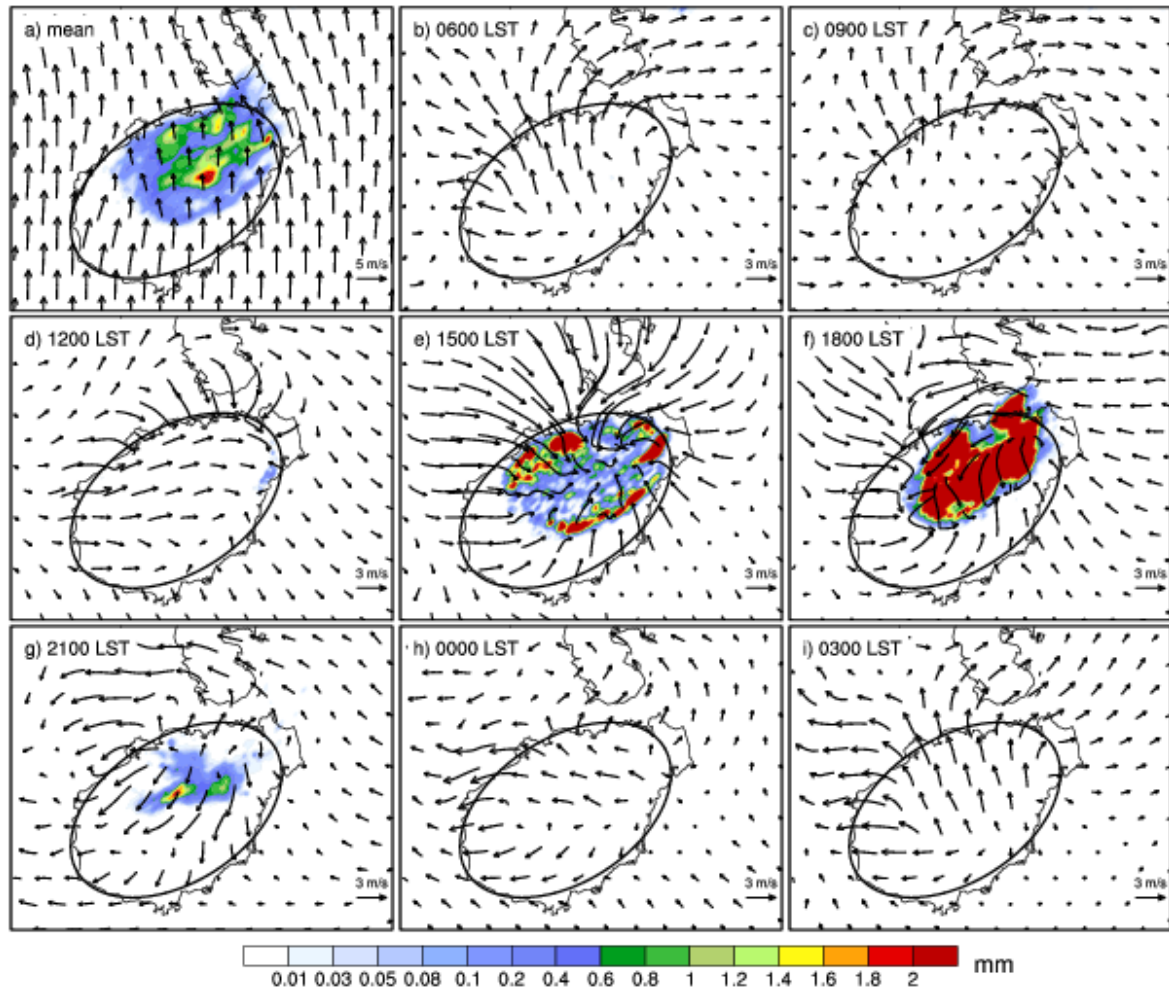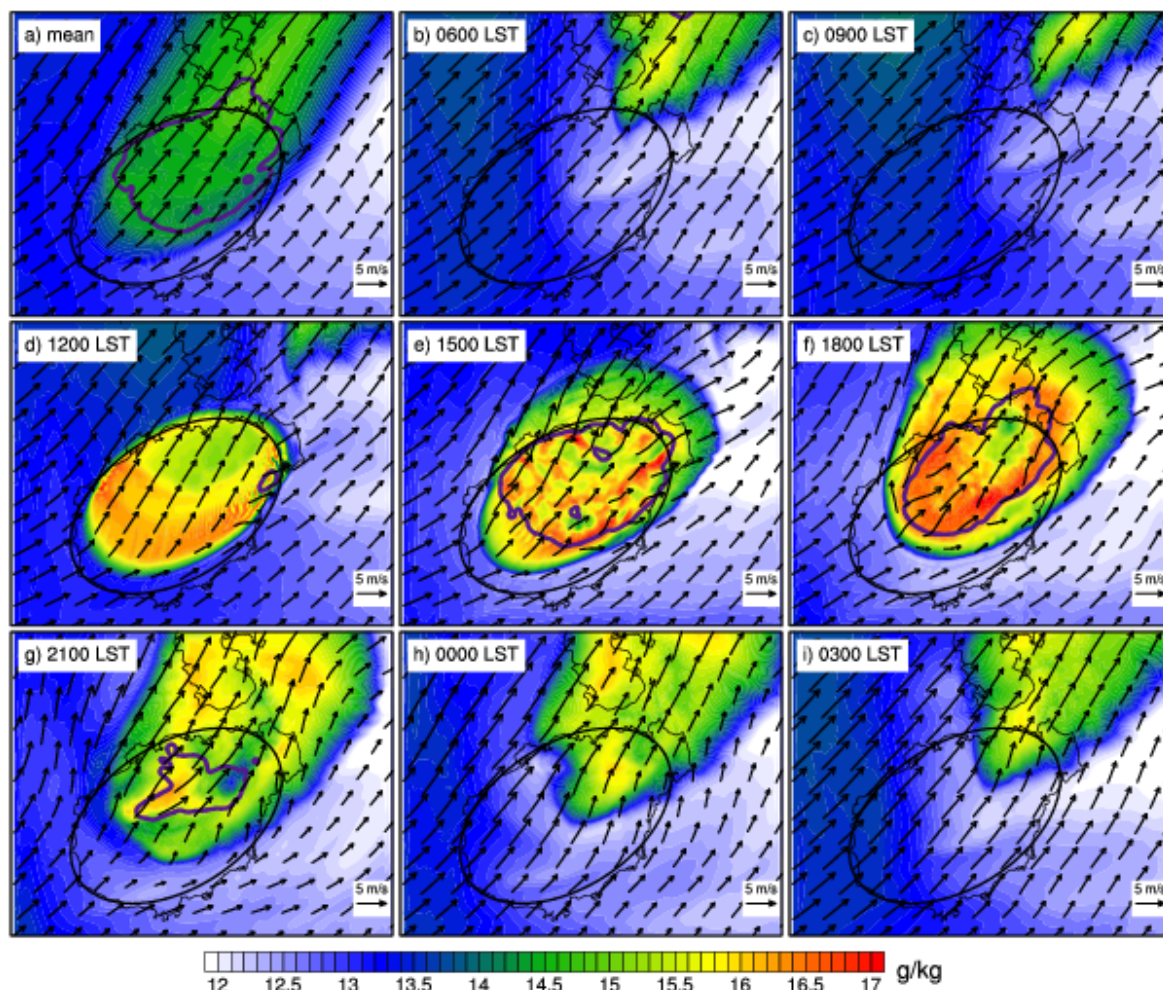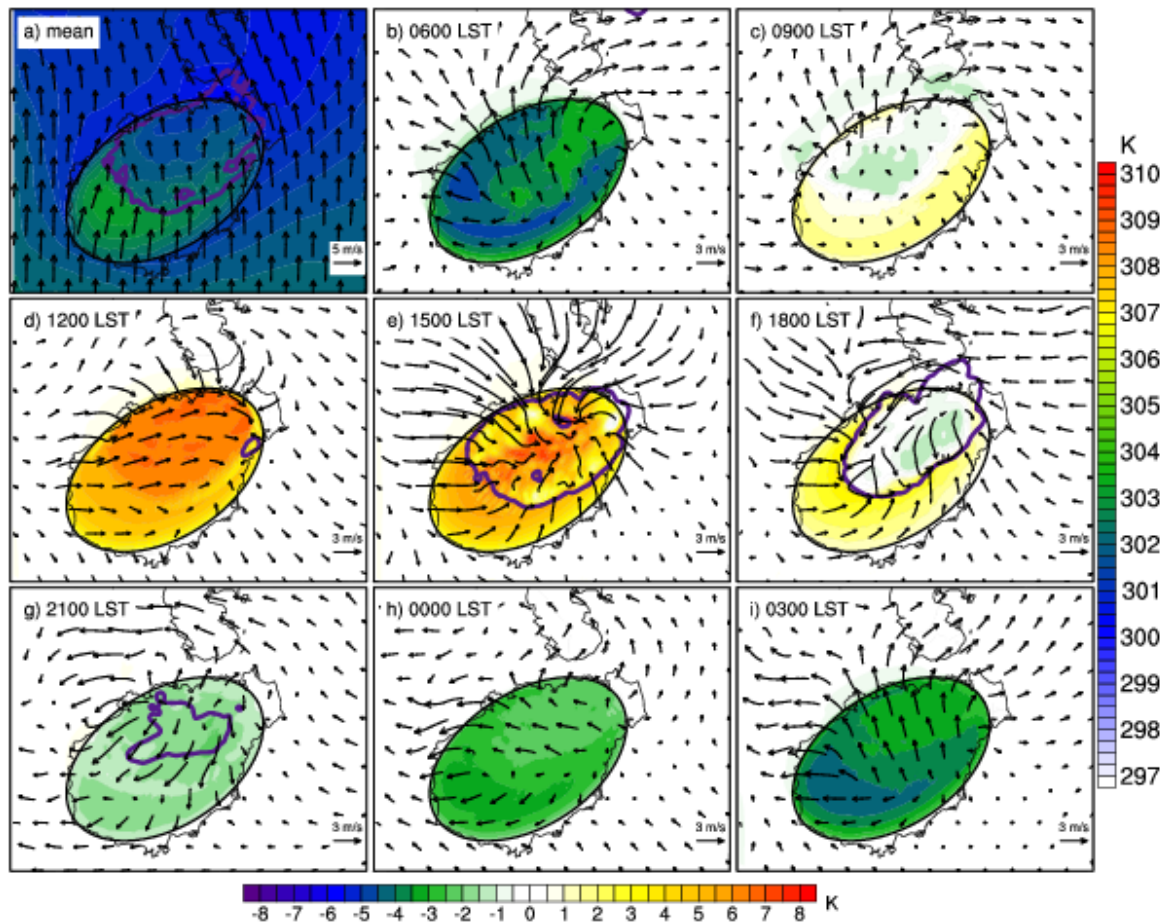
952
953
954
955
956
957
958
959
960
961

FIG. 12. (a) 2-meter mean temperature (shading) and horizontal wind (vectors) on the second lowest model level for horizontal wind; (b–i) 2-meter mean temperature perturbation (shading) and mean perturbation horizontal wind (vectors) on the second lowest model level every 3 h in IDEAL simulation. The right color bar is used for (a).
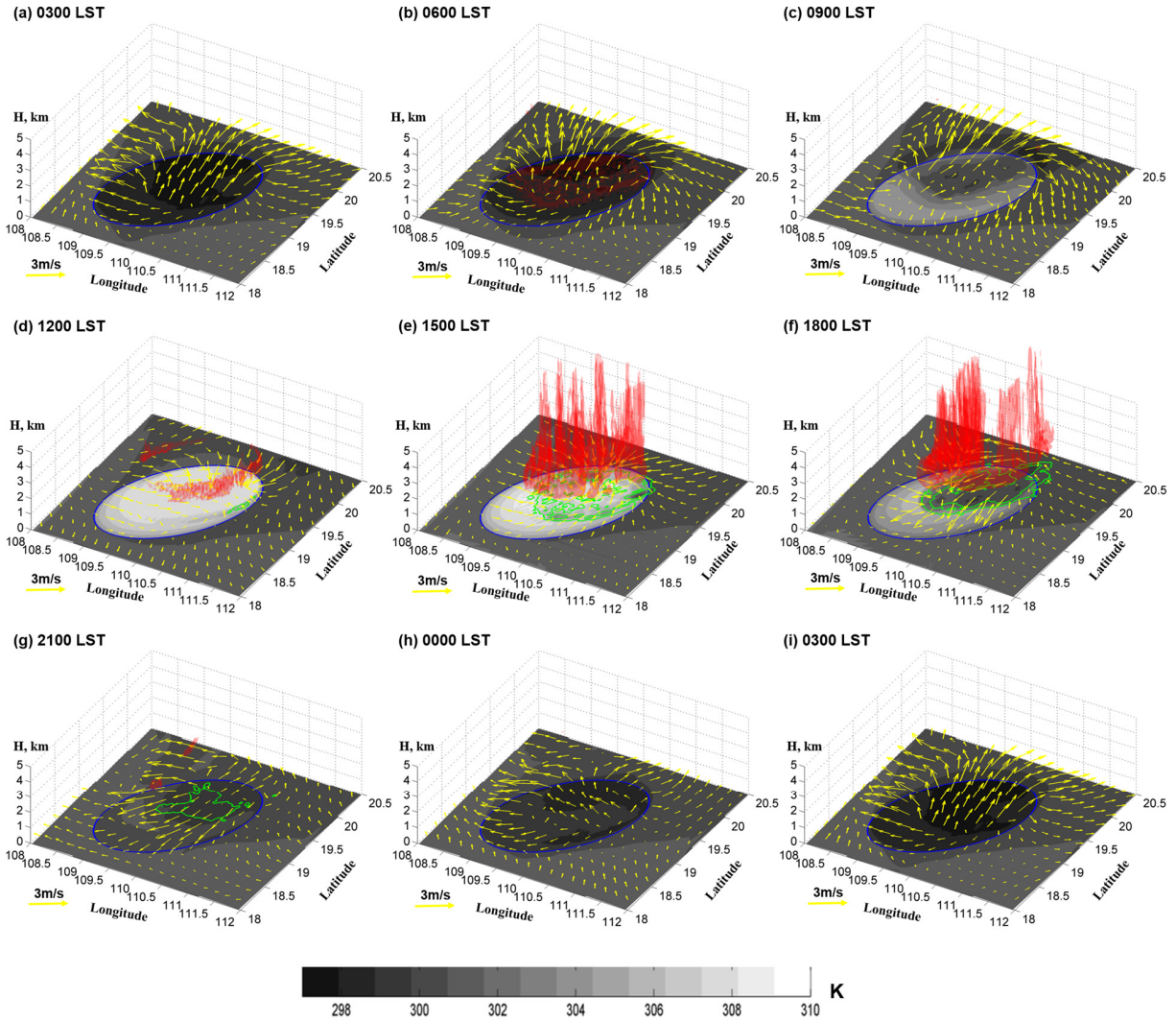
FIG. 13. Cloud water mixing ratio (red shading), 2-meter temperature (grey shaded), perturbation horizontal wind on the second lowest model level for horizontal wind (yellow vectors), and hourly precipitation accumulation (green contour lines) every 3 h in IDEAL simulation.
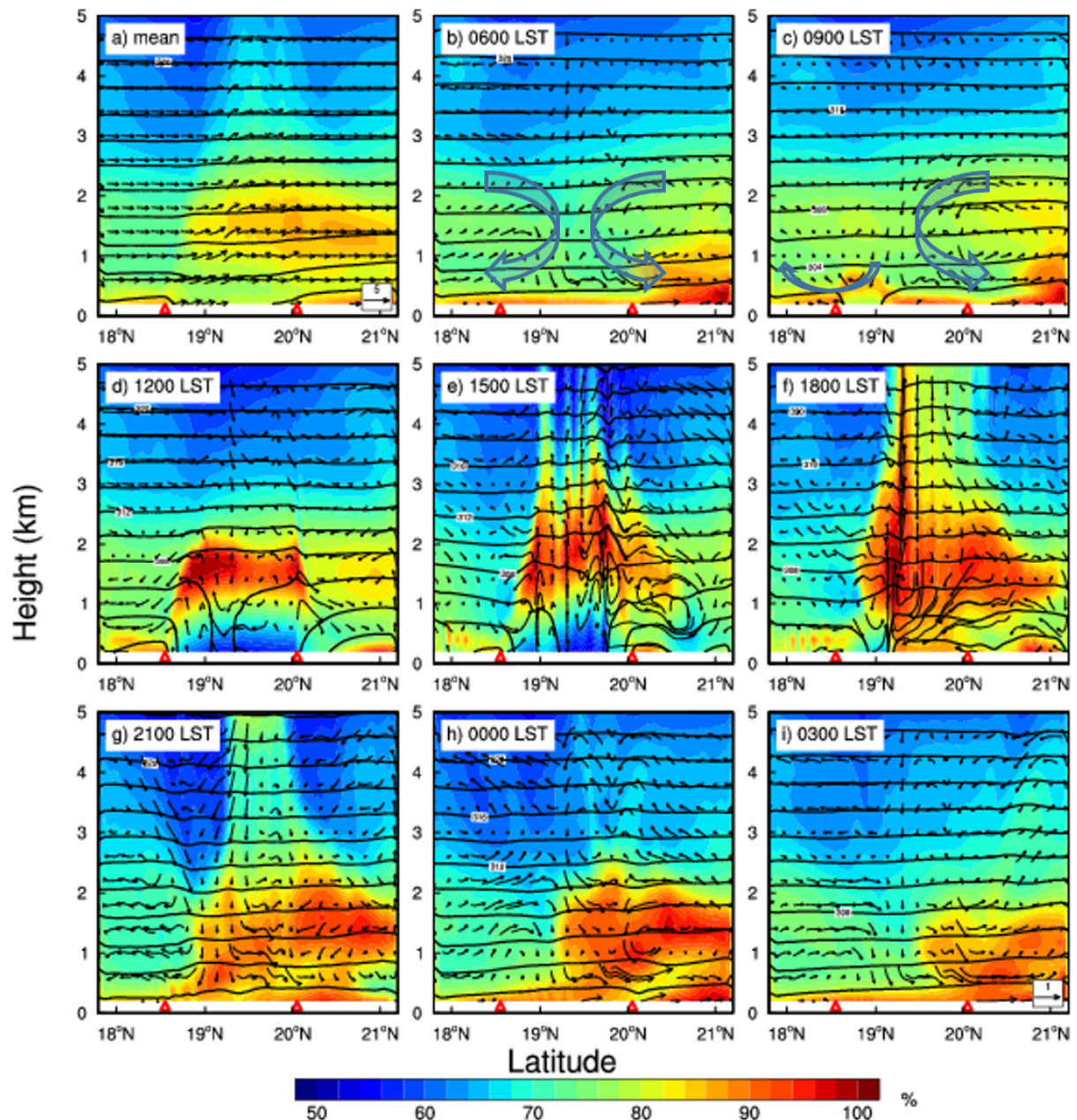
FIG. 14. Vertical cross-sections of relative humidity (shading), perturbation wind (vectors; the scale of the vertical component is increased by a factor of 5), and temperature (contours) in the south-to-north direction (see red line in Fig. 1) averaged over all hours (a) and at 3-h intervals (b–i) in IDEAL simulation. The triangles in each panel indicate the edges of the island. Arrows in b and c stand for the land breeze circulations.

1001
1002
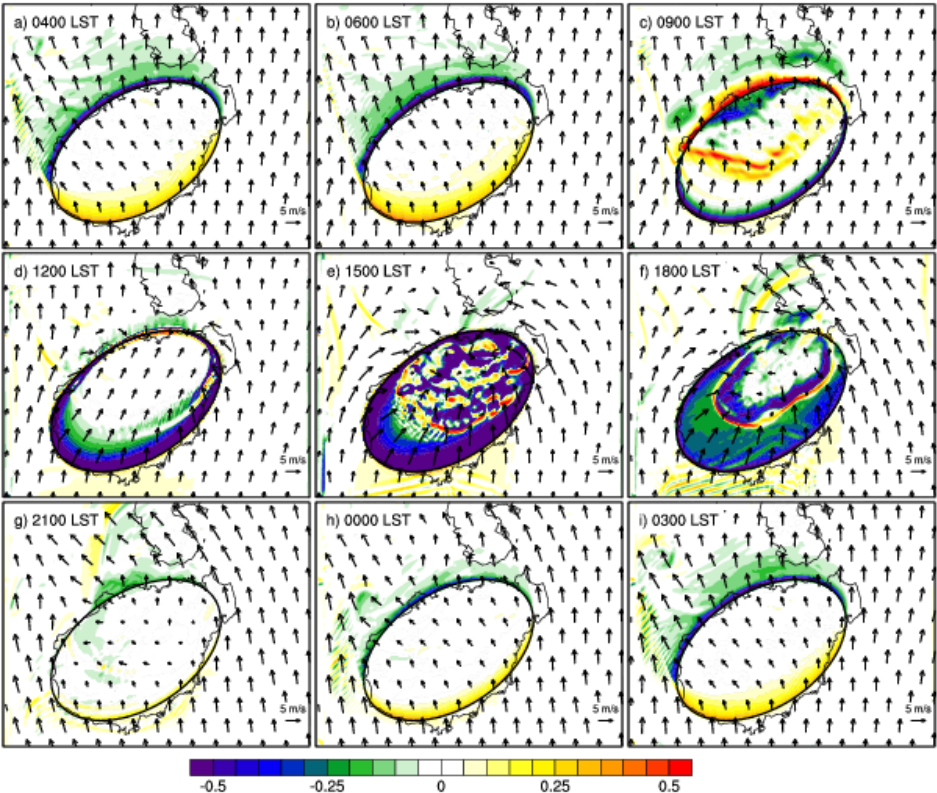
1003
1004 FIG. 15. Horizontal temperature advection (shaded) and horizontal wind (vector, m s^{-1}) on the
1005 first model level in simulation IDEAL.
1006
1007
1008
1009
1010
1011
1012
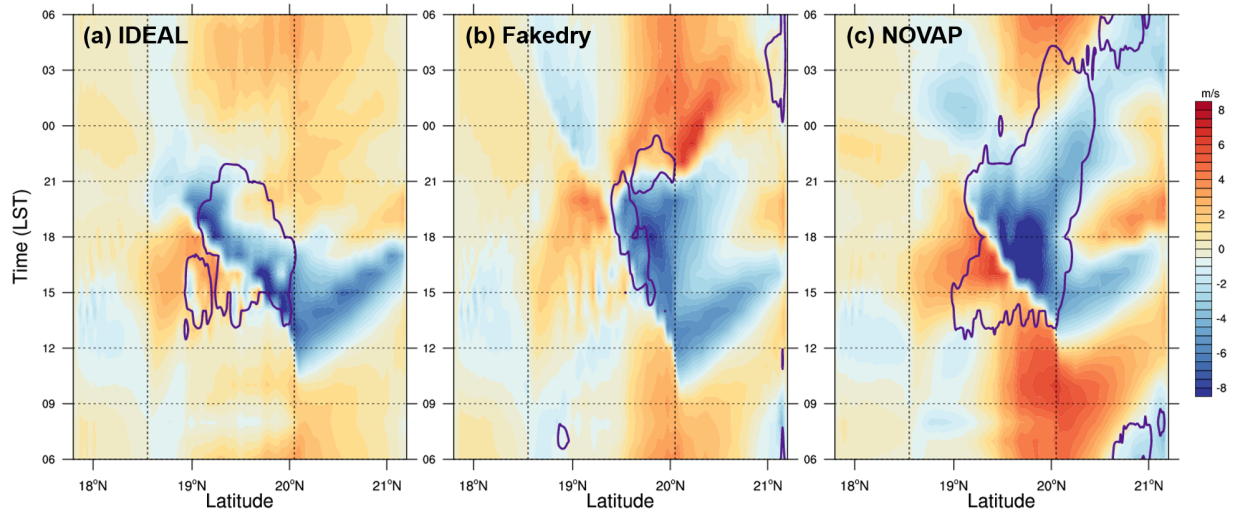
Fig. 16. Hovmoller diagrams of perturbation meridional wind component on the second lowest model level for horizontal wind (shading) in the (a) IDEAL, (b) Fakedry and (c) NOVAP simulations, respectively. Precipitation exceeding 0.1 mm h^{-1} is enclosed by the heavy purple contours. The two vertical dash lines indicate the edges of the island.